A&A 635, A118 (2020)
https://doi.org/10.1051/0004-6361/202037472

Astronomy & Astrophysics

Protostellar Outflows at the EarliesT Stages (POETS)

IV. Statistical properties of the 22 GHz H_2O masers

L. Moscadelli[1], A. Sanna[2,3], C. Goddi[4,5], V. Krishnan[1,6], F. Massi[1], and F. Bacciotti[1]

[1] INAF – Osservatorio Astrofisico di Arcetri, Largo E. Fermi 5, 50125 Firenze, Italy
e-mail: mosca@arcetri.astro.it
[2] INAF – Istituto di Radioastronomia & Italian ALMA Regional Centre, Via P. Gobetti 101, 40129 Bologna, Italy
[3] Max-Planck-Institut für Radioastronomie, Auf dem Hügel 69, 53121 Bonn, Germany
[4] Leiden Observatory, Leiden University, PO Box 9513, 2300 RA Leiden, The Netherlands
[5] Department of Astrophysics/IMAPP, Radboud University, PO Box 9010, 6500 GL, Nijmegen, The Netherlands
[6] South African Radio Astronomy Observatory (SARAO), 2 Fir street, Black River Park, Observatory, Cape Town 7925, South Africa

Received 9 January 2020 / Accepted 11 February 2020

ABSTRACT

Context. 22 GHz water masers are the most intense and widespread masers in star-forming regions. They are commonly associated with protostellar winds and jets emerging from low- and high-mass young stellar objects (YSO).
Aims. We wish to perform for the first time a statistical study of the location and motion of individual water maser cloudlets, characterized by typical sizes that are within a few au, with respect to the weak radio thermal emission from YSOs.
Methods. For this purpose, we have been carrying out the Protostellar Outflows at the EarliesT Stages survey of a sample (38) of high-mass YSOs. The 22 GHz water maser positions and three-dimensional (3D) velocities were determined through multi-epoch Very Long Baseline Array observations with accuracies of a few milliarcsec (mas) and a few km s^{-1}, respectively. The position of the ionized core of the protostellar wind, marking the YSO, was determined through sensitive radio continuum, multi-frequency *Jansky* Very Large Array observations with a typical error of ≈20 mas.
Results. The statistic of the separation of the water masers from the radio continuum shows that 84% of the masers are found within 1000 au from the YSO and 45% of them are within 200 au. Therefore, we can conclude that the 22 GHz water masers are a reliable proxy for locating the position of the YSO. The distribution of maser luminosity is strongly peaked towards low values, indicating that about half of the maser population is still undetected with the current Very Long Baseline Interferometry detection thresholds of 50–100 mJy beam^{-1}. Next-generation, sensitive (at the nJy level) radio interferometers will have the capability to exploit these weak masers for an improved sampling of the velocity and magnetic fields around the YSOs. The average direction of the water maser proper motions provides a statistically-significant estimate for the orientation of the jet emitted by the YSO: 55% of the maser proper motions are directed on the sky within an angle of 30° from the jet axis. Finally, we show that our measurements of 3D maser velocities statistically support models in which water maser emission arises from planar shocks with propagation direction close to the plane of the sky.

Key words. ISM: jets and outflows – ISM: molecules – masers – radio continuum: ISM – techniques: interferometric

1. Introduction

The 22 GHz water maser $6_{1,6}$–$5_{2,3}$ rotational transition is the most intense emission line at radio frequency and the most widespread interstellar maser. In star-forming regions, the average isotropic luminosity of detected water masers is $\sim 10^{-5}$ $L_\odot$ (Anglada et al. 1996, see Table 5) and in extreme cases, such as in the strong source W49N, it can be as high as ~ 1 $L_\odot$ (Elitzur et al. 1989). From the time of its discovery by Cheung et al. (1969), the water maser emission has been surveyed using both single-dish (Furuya et al. 2001; Felli et al. 2007; Urquhart et al. 2011; Walsh et al. 2011) and, more recently, connected interferometers (Beuther et al. 2002; Walsh et al. 2014; Titmarsh et al. 2016; Kim et al. 2019), with angular resolutions ranging from $\sim 1''$ to $\sim 1'$. These surveys have derived the global properties of the emission (luminosity, extent in LSR velocity ($V_{\rm LSR}$) and the time variability) of the interstellar water masers, in addition to studying the correlation with independent star-formation markers, particularly with other maser types. Very Long Baseline Interferometry (VLBI) observations of specific sources, achieving milliarcsecond (mas) angular resolution, allow us to resolve the emission and determine the spatial and spectral characteristics of individual maser cloudlets and measure their three-dimensional (3D) motion (Goddi et al. 2006). The VLBI results in most cases indicate a physical association of the water masers with protostellar winds and jets emerging from low- and high-mass young stellar objects (YSO; Torrelles et al. 2003; Moscadelli et al. 2005; Goddi & Moscadelli 2006; Sanna et al. 2012; Burns et al. 2016; Hunter et al. 2018).

Models of the 22 GHz water masers predict that the emission originates in warm and dense, shocked gas. Two different classes of shocks are considered: slow (≤40 km s^{-1}) non-dissociative C-type (Kaufman & Neufeld 1996), and fast (≥40 km s^{-1}) dissociative J-type (Elitzur et al. 1992; Hollenbach et al. 2013) shocks. The post-shock densities for water maser operation, H_2 number density ($n_{\rm H_2}$) $\sim 10^8$–10^9 cm^{-3}, are similar; however, in C shocks molecules are not dissociated and the masing gas attains high temperatures of 1000–2000 K, whereas in J-shocks, the H_2O

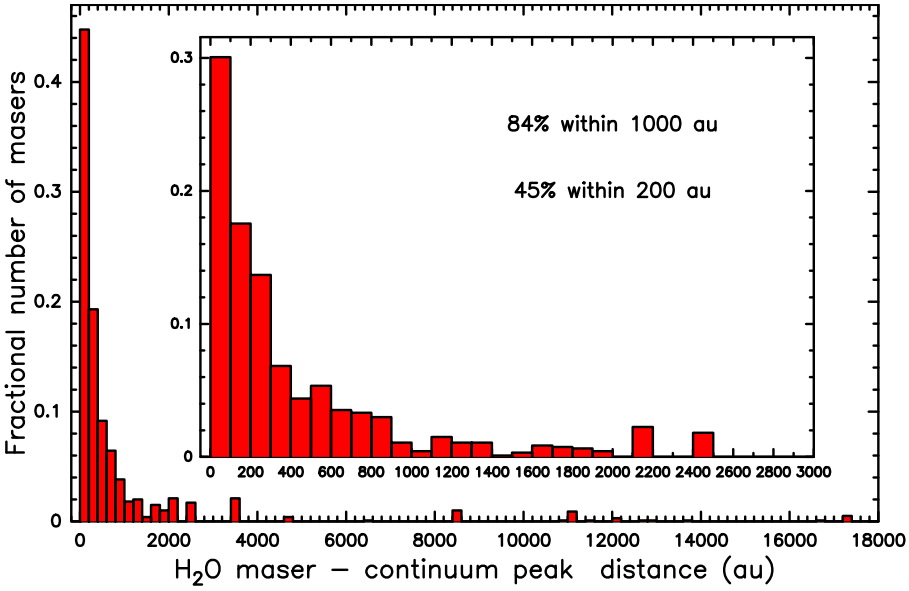

Fig. 1. Histograms of the sky-projected distance of water masers from the radio continuum peak, for all the observed masers in the POETS targets (main) and for a maximum continuum-maser separation of 3000 au (inset). Considering all the observed masers, the target-average distance error and corresponding standard deviation are 182 and 16 au, respectively. Selecting masers within 3000 au from the radio continuum peak, the target-average distance error and corresponding standard deviation are 108 and 17 au, respectively. Correspondingly, we used bins of 200 and 100 au for the histograms in the main plot and in the inset, respectively. The histogram values are normalized by the total number of selected water masers.

molecules reform in a post-shock temperature plateau of 400–500 K. Shocks are a natural by-product of winds and jets, caused either by a velocity or density change internal to the flow, or by interaction of the flow with the surrounding medium. The link between the water masers and the outflows from YSOs provided by the observations is, therefore, consistent with the shock models, although a more quantitative test of the models, in particular discerning between C- and J-shocks, is often hampered by insufficient knowledge about the flow geometry and its speed.

We have been carrying out the Protostellar Outflows at the EarliesT Stages (POETS) survey with the goal of imaging the inner outflow scales of 10–100 au in a statistically-significant sample (38[1]) of luminous YSOs, targeting both the molecular and ionized components of the outflows. The outflow kinematics is studied at mas scales through Very Long Baseline Array (VLBA) observations of the 22 GHz water masers belonging to the Bar and Spiral Structure Legacy survey (BeSSeL; see below). We have employed the *Jansky* Very Large Array (JVLA) at C- (6 GHz), Ku- (13 GHz), and K-band (22 GHz) in the A- and B-Array configurations (FWHM beams of 0.″1–0.″4) to determine the spatial structure and the spectral index of the radio continuum emission and to address its nature.

The BeSSeL survey is a key project of the VLBA, whose main goal is to derive the structure and kinematics of the Milky Way by measuring accurate positions, distances (via trigonometric parallaxes) and proper motions (PM) of 6.7 GHz methanol and 22 GHz water masers in hundreds of high-mass star forming regions distributed over the Galactic disk (Reid et al. 2014, 2019). The BeSSeL observations provide absolute positions and velocities of individual maser cloudlets with accuracies of a few mas and a few km s^{-1}, respectively, for hundreds of YSOs. They have an enormous value for star-formation studies since they afford for the first time a VLBI survey of the properties of the most widespread interstellar masers based on a large, homogeneous dataset.

Moscadelli et al. (2016; hereafter Mos16) presented the first results of the POETS survey for a pilot sample of 11 targets, also describing the target selection, observations, and data analysis. Sanna et al. (2018; hereafter Paper I) reported on and interpreted the radio continuum data of the whole sample, while Sanna et al. (2019a; hereafter Paper II) examined the radio synchrotron jet associated with the high-mass YSO G035.02+0.35. Moscadelli et al. (2019a; hereafter Paper III) completed the combined analysis of the radio continuum and water maser observations for all the targets, with a particular focus on the water maser kinematics. The main result of Paper III is that the 3D-velocity distribution of the water masers near the YSO in all the sources of the sample can be interpreted in terms of a single physical scenario: a disk-wind (DW). The observed masers are produced in the different regions of the DW, from the axial collimated jet portion to the wide-angle outer layers.

In this paper, we report on the statistics of the water maser properties and examine global correlations in the observed physical quantities. The distribution of water maser positions, luminosities, and 3D-velocity orientations and amplitudes is presented in Sect. 2. In Sect. 3, we discuss the use of the H_2O masers as a tool for star-formation studies. Our conclusions are presented in Sect. 4.

2. H_2O maser statistics

2.1. Distance from the YSO

In the POETS survey, on the basis of the spatial distribution of the water masers and their PMs, we could ascertain that 36 out of the 38 water masers observed with the JVLA are clearly associated with a radio continuum source. In Fig. 1, we analyze the linear separation of the detected water masers from the position of the radio continuum peak. In most of our targets, the continuum emission at both 13 and 22 GHz is dominated by a single (unresolved or slightly resolved) source, whose position is determined by fitting a 2D Gaussian profile. For each POETS target, we always select the radio continuum peak of the JVLA observation at the highest angular resolution, that is either 13 GHz or 22 GHz A-Array configuration. The histogram in the main plot of Fig. 1 considers all the water masers associated with the POETS targets, while the histogram in the inset only refers to masers up to a maximum separation of 3000 au from the continuum. Since the error on the linear distance is directly proportional to the distance at large values, the bins of the main and

[1] This number includes the two YSOs IRAS 20126+4104 and AFGL 5142 studied via multi-epoch VLBI observations by our group in the past, which have been added to the POETS sample of 36 targets (see Table A.1).

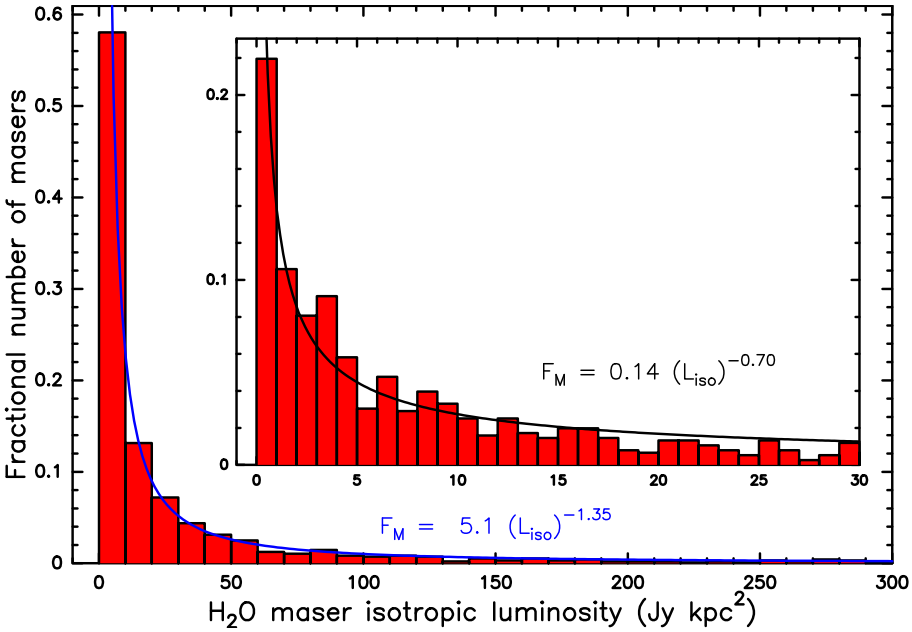

Fig. 2. Histograms of the maser isotropic luminosity for a maximum maser luminosity of 300 Jy kpc^2 (main) and 30 Jy kpc^2 (inset). Less than 4% of the observed masers have an isotropic luminosity higher than 300 Jy kpc^2. The bins are 10 and 1 Jy kpc^2 for the histograms in the main plot and in the inset, respectively. The histogram values are normalized by the total number of selected water masers. The continuous blue and black lines show the power-law fits of the values of the histograms in the main plot and in the inset, respectively, and the best-fit expressions are also reported using the same colors of the corresponding fits.

inset histograms are chosen 200 and 100 au, respectively, which is comparable with the average distance error of the selected masers. The histogram value is the fractional number of water masers in a bin. From these plots we infer that 84% of the water masers are found within 1000 au from the radio continuum peak and 45% within 200 au.

As discussed in Mos16, the peak of the radio continuum at 13 or 22 GHz is a good proxy for the YSO position, within the absolute position accuracy of ≈20 mas of JVLA observations. This belief is supported by several facts ascertained for the large majority of our targets: (1) the peaks of the radio continuum at 6, 13, and 22 GHz coincide in position within the errors and the determined radio spectral index, in the range of −0.1 – 1.3, is consistent with thermal bremsstrahlung from a YSO wind; (2) the water masers are distributed across the radio continuum at separations ≤1000 au from the continuum peak; (3) the water maser 3D velocities are best interpreted in terms of a DW emerging from the YSO (see Paper III). Therefore, on the basis of the distance distribution from the continuum shown in Fig. 1, we are able to statistically assess for the first time that water masers can be efficiently used to pinpoint the position of a YSO with an uncertainty of a few 100 au. We discuss this result in the context of the relevant literature in Sect. 3.1. Table A.1 lists the POETS targets, reporting distance, bolometric luminosity, YSO position pinpointed by the radio continuum, number of detected maser cloudlets, and the maximum maser separation from the YSO.

2.2. Isotropic luminosity

Most of the water masers detected in the POETS survey have their peak intensity in the range of 0.05–50 Jy beam^{-1}. The isotropic luminosity, $L_{\rm iso}$, of a maser cloudlet is calculated with the product $L_{\rm iso} = F_{\rm p} D^2$, where $F_{\rm p}$ is the (Gaussian-fit) flux of the strongest emission channel, averaged over the different observing epochs, and D is the source distance. The large majority, that is, 96%, of the masers, have $L_{\rm iso} \leq 300$ Jy kpc^2, although exceptionally bright masers with $L_{\rm iso} \sim 10^3$–10^4 Jy kpc^2 have also been observed. The histograms in Fig. 2 show that the distribution of maser luminosity is strongly peaked towards low values: in considering masers with $L_{\rm iso} \leq 300$ Jy kpc^2, 86% of them have $L_{\rm iso} \leq 50$ Jy kpc^2; taking the masers with $L_{\rm iso} \leq 30$ Jy kpc^2, 56% of them have $L_{\rm iso} \leq 5$ Jy kpc^2. The implications of this luminosity distribution for more sensitive water maser observations of the future are considered in Sect. 3.2.

2.3. 3D velocities

Combining the water maser PM and line of sight (LOS) velocity, we derive the maser 3D velocity. We have been searching the literature for the systemic $V_{\rm LSR}$ of our targets from observations of high-density ($n_{\rm H_2} \geq 10^6$ cm^{-3}) thermal tracers and, in most cases, the found values are accurate within a few km s^{-1}. Since PMs are determined with comparable accuracies of a few km s^{-1} (see Tables 6–16 in Mos16, and Tables B1–B27 in Paper III), we estimate an average error on the 3D-velocity amplitude of 3.3 km s^{-1}. The histogram of the maser 3D-velocity amplitudes is presented in Fig. 3, from which it is clear that a large fraction, 63%, of the water maser speeds falls in the range 10–30 km s^{-1}.

It is also interesting to study the angular distribution of the maser 3D velocities, considering both their projection into the plane of the sky and their inclination with respect to it. In Paper III (see Figs. C1–C3), we produced histograms of the position angle (PA) of the water maser PMs for all the targets with at least two measured PMs and studied the degree of collimation of the maser velocities in the plane of the sky. In searching the literature for high-angular ($\lesssim 1''$) resolution observations in thermal continuum and line tracers of our targets, for several cases we were able to ascertain the PA of the (sky-projected) axis of the YSO jet, referred to as $A_{\rm LJ}$ (see Paper III, Table A.1). Figure 4 presents the histogram of the difference between the maser PM PA and $A_{\rm LJ}$, cumulating all the 14 POETS targets for which the direction of the protostellar jet is known from the literature (see Paper III, Table A.1). The average error on the PM PA is about half of the histogram bin. We note that 55% of the PMs of the masers is directed on the sky within an angle of 30° from the jet axis.

In Fig. 5 we have plotted the histogram of the inclination of the 3D velocities with the plane of the sky for all the water masers with measured PMs. The histogram bin is comparable with the average error of the inclination. It is clear that most of

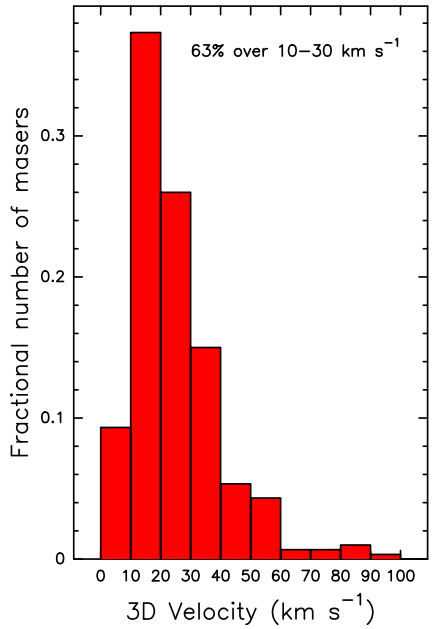

Fig. 3. Histogram of the maser 3D-velocity amplitude, cumulating all the POETS targets. The histogram bin is 10 km s^{-1} and the histogram values are normalized by the total number of masers with measured PMs. The average error on the 3D-velocity amplitude and corresponding standard deviation are 3.3 and 2.5 km s^{-1}.

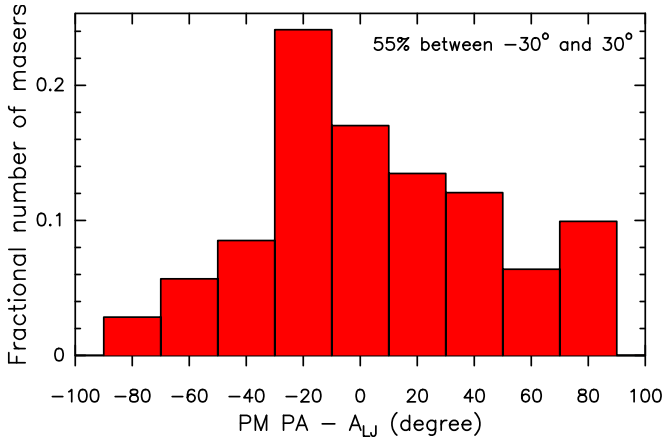

Fig. 4. Histogram of the difference between the maser PM PA and the PA of the jet axis from the literature, A_{LJ}, cumulating all the 14 POETS targets in which a jet has been observed through thermal tracers (see Table A.1 of Paper III). The histogram bin is 20° and the histogram values are normalized by the total number of considered PMs. The target-average error on the PM PA and corresponding standard deviation are 12° and 4°.

the observed water masers move close to the plane of the sky, 92% and 62% within an angle of 35° and 15°, respectively.

3. Discussion

3.1. H_2O masers marking the YSOs

The result presented in Sect. 2.1 is derived from absolute positions (accurate to a few mas) of 994 individual maser cloudlets associated with 36 distinct YSOs (see Table A.1), whose position on the sky and distance are determined with an accuracy of a few 10 mas and 5–10% (via maser trigonometric parallax measurements), respectively. The mas-level accuracy in our VLBI

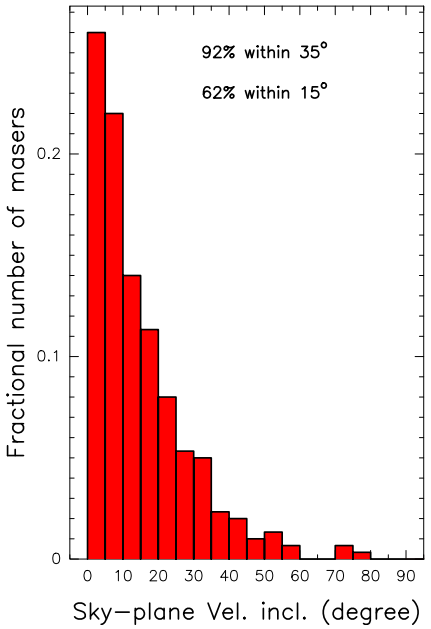

Fig. 5. Histogram of the inclination of the 3D water maser velocity with the plane of the sky, cumulating all the POETS targets. The histogram bin is 5° and the histogram values are normalized by the total number of masers with measured PMs. The average error on the maser velocity inclination and corresponding standard deviation are 7° and 4°.

H_2O maser positions together with the employment of a reliable YSO tracer (i.e., sensitive, rms∼10 μJy beam^{-1}, JVLA A-Array observations) distinguishes ours from previous surveys of interstellar water masers, such as those by Beuther et al. (2002), Walsh et al. (2014), Titmarsh et al. (2016), and Kim et al. (2019). These former surveys were conducted with connected element interferometers (Very Large Array, VLA; Australian Telescope Compact Array, ATCA; Korean VLBI Network, KVN) achieving an angular resolution of $\geq$ 0.″1, which is insufficient for determining the spatial and velocity distribution of individual maser cloudlets.

In these previous surveys, a significant fraction of the water masers is always found to be offset by a few arcsec from the complementary star formation indicators (such as mm-continuum sources and 6.7 GHz CH_3OH masers), calling into question the connection between the water masers and a specific phase of the YSO evolution. This apparent discrepancy can be readily explained by limitations of previous surveys, including poor resolution and sensitivity (typically an order of magnitude worse than POETS for the radio continuum). At 22 GHz, the radio continuum sensitivity of the POETS survey (∼30 μJy over a beam size of 0.″1) allows us to detect the flux from an unresolved, optically thin, HII region excited by a zero-age main-sequence (ZAMS) star with spectral type as late as B5 at a distance of 1 kpc, and B3–B4 at 3–4 kpc. Therefore, sensitive JVLA A-Array continuum observations towards the water masers detected in these previous surveys would provide a critical test of our results by searching for previously undetected cluster components emitting (free–free) radio continuum. Indeed, our results clearly indicate a strong connection between the water masers and an active phase of mass ejection (and accretion) of the YSO.

3.2. The H_2O maser brightness function

We do not find any clear correlation between the intensity of the water maser and its distance from the YSO or its

3D-velocity amplitude. In general, water masers cluster on scales of ∼10 au and it is quite common to find mixed groups of intense and weak masers at similar distance from the YSO. This qualitatively agrees with the shock models for the origin of the H_2O masers, which predict that the peak flux of the masers depends mostly on the LOS velocity coherent, amplification path (Hollenbach et al. 2013, Eq. (14)) in the post-shock gas layers. Then, a large range of maser amplification paths (and intensities) across small regions is naturally expected since: (1) both the density and velocity behind shocks vary on very small scales, namely, ≤1 au (Hollenbach et al. 2013, see Fig. 4); (2) the shock velocities can be inclined at different angles with respect to the LOS; (3) depending on the very local conditions of the ambient medium, shocks can even become fragmented and dissipate. In this way, the scatter in maser intensities owing to the specific shock geometry can conceal a weaker dependence of the maser intensity on the position from the YSO and the shock speed.

The histograms of Fig. 2 indicate that the channel-map detection threshold of ∼100 mJy beam^{-1} of present spectroscopic VLBI measurements is insufficient to adequately image the water maser emission associated with YSOs. In fact, the steep increase of the fractional number of detected masers with decreasing luminosity strongly suggests that there is a multitude of masers with an intensity ≤100 mJy beam^{-1} remaining undetected. In Fig. 2, we report the power-law fits of the histogram values both for the main plot and the inset. We have to consider that the first bins of these histograms are certainly underestimated owing to our limited sensitivity. It should also be noted that the fitted power-law expressions reported in Fig. 2 are not normalized. Requiring that the integral between $0 \leq L_{\rm iso} \leq 30$ Jy kpc^2 be equal to 1, we determine the corrected brightness distribution for weak water masers as:

$$F_{\rm M} = 0.11\ (L_{\rm iso})^{-0.70}. \quad (1)$$

Equation (1) implies that about 50% of the whole water maser population have a luminosity that is less than the typical detection threshold of a few Jy kpc^2 and it is still undetected. The next-generation VLA (ngVLA) will be the appropriate facility to study the spatial and velocity distribution of this large family of weaker masers (Hunter et al. 2018), which can be used to sample the 3D-velocity field around the forming YSO with much better detail. If water masers at a distance of ≲1000 au from the YSOs trace magneto-centrifugal DWs (see Paper III), multi-epoch ngVLA, polarized 22 GHz maser observations can serve as a unique tool to investigate both the velocity and magnetic fields of DWs. Moreover, the ngVLA will permit a simultaneous study of the water masers and the (usually faint) radio continuum of the YSO, improving the precision of the maser positions (and velocities) in the YSO reference frame.

3.3. The origin of H_2O masers in shocks

Concerning the statistics on the properties of the H_2O maser 3D velocities, the first notable result is the global distribution of the PM directions with respect to the orientation of the YSO jet, presented in Fig. 4. The fact that more than half of the observed PMs is oriented on the sky within an angle of 30° from the jet axis implies that, statistically, the observation of only a few maser PMs associated with a given YSO can already suffice to constrain the direction of the protostellar jet. In the literature, there have been several studies published on specific sources assessing that water masers can be reliable tracers of the YSO outflows (see Sect. 1 for references), but our H_2O maser survey first provides a statistic of the water maser PM directions based on a relatively large sample of targets. Figure 4 can also be read that about half of the water masers move along directions forming large angles with the jet. The non-collimated motion, near the YSO, of half of the water masers has been interpreted in Paper III in terms of a wide-angle velocity pattern associated with the outer, less collimated portion of the DW.

The second interesting result is the finding that almost all the measured maser 3D velocities form small angles (≤35°) with the plane of the sky, as indicated by the histogram in Fig. 5. That agrees very well with the shock models for the water masers (Elitzur et al. 1992; Kaufman & Neufeld 1996; Hollenbach et al. 2013), where a long velocity-coherent, amplification path along the LOS is predicted for planar shocks with propagation direction close to the plane of the sky. In this case, there are no large variations of the velocity along the LOS, which permits the formation of intense masers. Therefore, we can explain the histograms in Fig. 5 as an observational bias, given that masers moving at small (large) angles from the plane of the sky have a much higher (lower) detection probability.

In the following, we discuss in more detail the properties of the shocks excited in protostellar winds that can serve as the birthplaces of the H_2O masers. Let us indicate with $V_{\rm w}$ and $\rho_{\rm w}$ the speed and the density, respectively, of the wind, and with $V_{\rm u}$ and $\rho_{\rm u}$ the speed and the density, respectively, of the pre-shock material on which the wind impinges, that is $V_{\rm w} \geq V_{\rm u}$. Both for radiative and adiabatic shocks, the shock velocity, $V_{\rm s}$, approximated by the water maser velocity, can be written as (Masson & Chernin 1993, see Eqs. (3) and (4)):

$$V_{\rm s} \approx V_{\rm u} + \frac{V_{\rm w} - V_{\rm u}}{1 + \sqrt{\rho_{\rm u}/\rho_{\rm w}}}. \quad (2)$$

According to the shock models, H_2O masers originate in post-shock gas layers with (H_2 number) density of $n_{\rm H_2} \sim 10^8$–10^9 cm^{-3} (Hollenbach et al. 2013). These high post-shock densities can be obtained either behind weak C shocks propagating through very dense regions, $\rho_{\rm u} \sim 10^8$–10^9 cm^{-3}, $5 \leq (V_{\rm s} - V_{\rm u}) \leq 40$ km s^{-1}, or behind strong J shocks crossing less dense gas, $\rho_{\rm u} \sim 10^6$–10^7 cm^{-3}, $(V_{\rm s} - V_{\rm u}) \geq 50$ km s^{-1}.

Gas densities as high as 10^8–10^9 cm^{-3} are typical of the few disks discovered around high-mass YSOs (Beuther et al. 2013; Johnston et al. 2015; Ilee et al. 2016; Moscadelli et al. 2019b; Sanna et al. 2019b). DWs are expected to be launched from the surface of such dense disks (Pudritz & Banerjee 2005; Kölligan & Kuiper 2018). On the basis of Eq. (2), weak, internal C shocks in the slower and less collimated regions of DWs, with $\rho_{\rm w} \approx \rho_{\rm u} \sim 10^8$–$10^9$ cm^{-3}, and $10\ {\rm km\ s^{-1}} \leq V_{\rm u} \lesssim V_{\rm w} \leq 40\ {\rm km\ s^{-1}}$, would propagate at speeds of 10–30 km s^{-1}, in good agreement with the peak of the velocity distribution of the water masers shown in Fig. 3. Therefore, based on the analysis of the direction and amplitude of the maser velocities, we suggest that about 50% of the water masers, excited within 1000 au from the YSOs, originate in C shocks internal to DWs.

The highest maser speeds, ≥30 km s^{-1}, of the distribution of Fig. 3 could instead be generated in strong J shocks, which are naturally expected to be associated with fast protostellar jets. The radio continuum emission from thermal jets is thought to be produced in internal shocks and provides a reliable way to estimate the jet properties. At 100–1000 au from the YSOs, typical jet speeds and densities are $V_{\rm w} \approx$ 100–1000 km s^{-1} and $\rho_{\rm w} \sim 10^6$ cm^{-3}, respectively (Anglada et al. 2018; Rosero et al. 2019). If such fast jets impact denser, $\rho_{\rm u} \approx 10^7$–$10^8$ cm^{-3}, stationary, $V_{\rm u} \approx 0$ km s^{-1}, ambient material, Eq. (2) predicts velocities

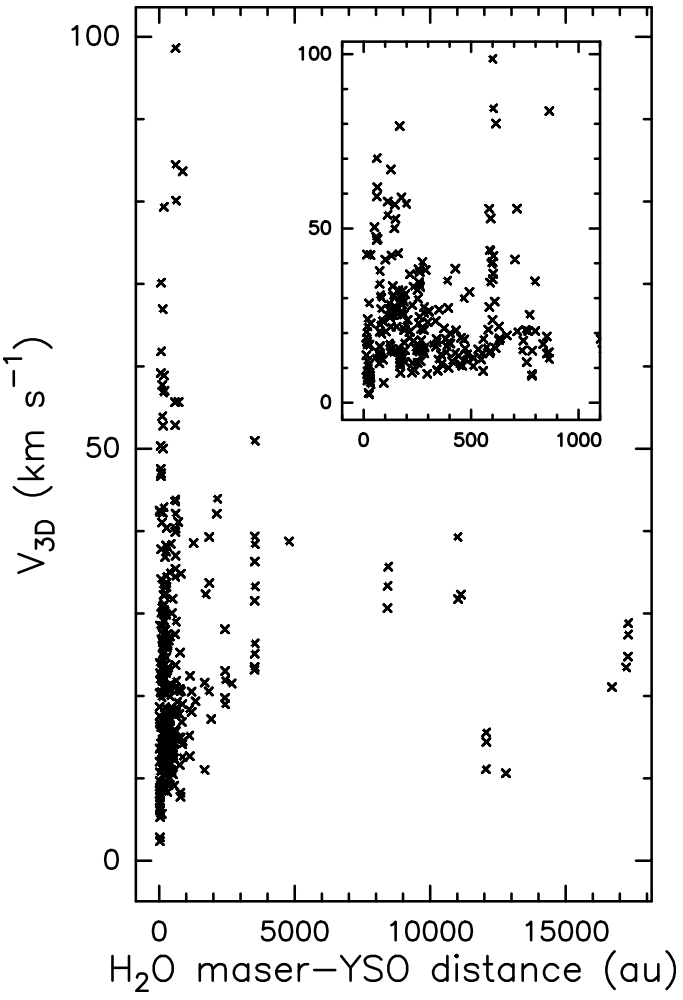

Fig. 6. Amplitude of the 3D velocities of the H_2O masers vs. the distance from the YSO, cumulating all the POETS targets. The inset in the upper right corner shows an enlargement of the main plot for the distance range 0–1100 au.

for the shocks a factor of 3–10 smaller than that of the jet, in agreement with our measurements for the faster subset of water masers. Thus, we propose that the water masers showing higher velocities, that is, ≥30 km s^{-1}, or larger separation, at several 1000 au, from the YSO originate in J shocks owing to the interaction of the protostellar jet with the surrounding material.

Figure 6 presents the distribution of the 3D-velocity amplitude of the water masers versus the distance from the YSO. In particular, the plot in the inset shows that the large majority of the masers within 1000 au have speeds ≤30 km s^{-1}, and, following our interpretation, it should originate in internal C shocks of the YSOs DWs. Considering, instead, the near, ≤1000 au, fastest, ≥30 km s^{-1}, masers, we note that a significant fraction of them are found within 200 au from the YSO. The plot of Fig. 6 cumulates all the POETS targets, covering a large range in bolometric luminosities, 10^2–10^5 $L_\odot$, and YSO masses, 5–30 $M_\odot$. A corresponding large variation in the sizes of the kinematic structures (i.e., disks, DWs and jets) surrounding the YSOs is also expected. Then, the plot region ≤200 au and ≥30 km s^{-1} could correspond to water masers associated with the roots of the jets in lower-mass YSOs. Inspecting the main plot of Fig. 6, it is also remarkable that the minimum water maser velocity increases regularly with the distance from the YSO up to, at least, 4000–5000 au. Following our discussion, at separations of 1000–10000 au, water masers should mainly arise in J shocks excited in the jet-ambient interaction, and, on the basis of Eq. (2), a plausible interpretation is that the shock (and maser) velocities increase because the jet is continuously accelerated at this range of distances (Pudritz et al. 2007; Ramsey & Clarke 2019).

4. Conclusions

This paper presents a statistical analysis of the kinematic properties at mas resolution of a large sample of 994 H_2O masers, associated with 36 distinct YSOs. To our knowledge, this is the first VLBI survey of the 22 GHz H_2O masers, including a sizable number of sources and based on maser positions and 3D velocities determined with an accuracy of a few mas and a few km s^{-1}, respectively. The main results can be summarized as follows:

1. The 22 GHz water masers are a reliable proxy for the position of the YSOs: 84% of them are found within 1000 au from the YSO, and 45% within 200 au.
2. The distribution of maser luminosity is strongly peaked towards low values, indicating that about half of the maser population, with intensities ≤100 mJy beam^{-1}, remains undetected.
3. The PA of the water maser PMs provides a statistically-significant estimate for the PA of the YSO jet: 55% of the maser PMs are directed on the sky within an angle of 30° from the jet axis.
4. The 3D maser velocities have small (≤35°) inclinations with the plane of the sky and amplitudes mainly in the range of 10–30 km s^{-1}.

Regarding point 2, future sensitive interferometers (e.g., ngVLA) will serve as the appropriate instruments for studying the weaker, albeit conspicuous, water maser population predicted in this work. Concerning points 3 and 4, we stress that for the first time we are providing a statistic for the amplitude and directions of 3D velocities for the 22 GHz water masers. We find that water masers moving almost parallel to the plane of the sky are preferentially detected. This result fully supports the shock models for the origin of the water masers, where a long velocity-coherent, amplification path along the LOS is predicted for planar shocks with propagation direction close to the plane of the sky. In Paper III, which focused on the maser kinematics, we proposed that the water masers near the YSOs trace the different regions of a DW, from the fast and collimated jet portion to the slower, wide-angle outer layers. Following this interpretation, we can now make a prediction on the nature of the maser shocks. While most of the water masers with lower speed, that is, ≤30 km s^{-1}, should be excited in weak, internal C shocks occurring in the slower regions of the DWs, most of the masers at higher velocity, that is, ≥30 km s^{-1}, should originate in strong J shocks wherever the fast jets hit the ambient medium.

References

Anglada, G., Estalella, R., Pastor, J., Rodriguez, L. F., & Haschick, A. D. 1996, ApJ, 463, 205
Anglada, G., Rodríguez, L. F., & Carrasco-González, C. 2018, A&ARv, 26, 3
Beuther, H., Walsh, A., Schilke, P., et al. 2002, A&A, 390, 289
Beuther, H., Linz, H., & Henning, T. 2013, A&A, 558, A81
Burns, R. A., Handa, T., Nagayama, T., Sunada, K., & Omodaka, T. 2016, MNRAS, 460, 283
Cheung, A. C., Rank, D. M., Townes, C. H., Thornton, D. D., & Welch, W. J. 1969, Nature, 221, 626
Elitzur, M., Hollenbach, D. J., & McKee, C. F. 1989, ApJ, 346, 983
Elitzur, M., Hollenbach, D. J., & McKee, C. F. 1992, ApJ, 394, 221

Felli, M., Brand, J., Cesaroni, R., et al. 2007, A&A, 476, 373
Furuya, R. S., Kitamura, Y., Wootten, H. A., Claussen, M. J., & Kawabe, R. 2001, ApJ, 559, L143
Goddi, C., & Moscadelli, L. 2006, A&A, 447, 577
Goddi, C., Moscadelli, L., Torrelles, J. M., Uscanga, L., & Cesaroni, R. 2006, A&A, 447, L9
Hollenbach, D., Elitzur, M., & McKee, C. F. 2013, ApJ, 773, 70
Hunter, T. R., Brogan, C. L., Bartkiewicz, A., et al. 2018, ASP Conf. Ser., 517, 321
Ilee, J. D., Cyganowski, C. J., Nazari, P., et al. 2016, MNRAS, 462, 4386
Johnston, K. G., Robitaille, T. P., Beuther, H., et al. 2015, ApJ, 813, L19
Kaufman, M. J., & Neufeld, D. A. 1996, ApJ, 456, 250
Kim, W.-J., Kim, K.-T., & Kim, K.-T. 2019, ApJS, 244, 2
Kölligan, A., & Kuiper, R. 2018, A&A, 620, A182
Masson, C. R., & Chernin, L. M. 1993, ApJ, 414, 230
Moscadelli, L., Cesaroni, R., & Rioja, M. J. 2005, A&A, 438, 889
Moscadelli, L., Sánchez-Monge, Á., Goddi, C., et al. 2016, A&A, 585, A71
Moscadelli, L., Sanna, A., Goddi, C., et al. 2019a, A&A, 631, A74
Moscadelli, L., Sanna, A., Cesaroni, R., et al. 2019b, A&A, 622, A206
Pudritz, R. E., & Banerjee, R. 2005, IAU Symp., 227, 163
Pudritz, R. E., Ouyed, R., Fendt, C., & Brandenburg, A. 2007, in Protostars and Planets V, eds. B. Reipurth, D. Jewitt, & K. Keil (Tuson: University of Arizona Press), 277
Ramsey, J. P., & Clarke, D. A. 2019, MNRAS, 484, 2364
Reid, M. J., Menten, K. M., Brunthaler, A., et al. 2014, ApJ, 783, 130
Reid, M. J., Menten, K. M., Brunthaler, A., et al. 2019, ApJ, 885, 131
Rosero, V., Hofner, P., Kurtz, S., et al. 2019, ApJ, 880, 99
Sanna, A., Reid, M. J., Carrasco-González, C., et al. 2012, ApJ, 745, 191
Sanna, A., Moscadelli, L., Goddi, C., Krishnan, V., & Massi, F. 2018, A&A, 619, A107
Sanna, A., Moscadelli, L., Goddi, C., et al. 2019a, A&A, 623, L3
Sanna, A., Kölligan, A., Moscadelli, L., et al. 2019b, A&A, 623, A77
Titmarsh, A. M., Ellingsen, S. P., Breen, S. L., Caswell, J. L., & Voronkov, M. A. 2016, MNRAS, 459, 157
Torrelles, J. M., Patel, N. A., Anglada, G., et al. 2003, ApJ, 598, L115
Urquhart, J. S., Morgan, L. K., Figura, C. C., et al. 2011, MNRAS, 418, 1689
Walsh, A. J., Breen, S. L., Britton, T., et al. 2011, MNRAS, 416, 1764
Walsh, A. J., Purcell, C. R., Longmore, S. N., et al. 2014, MNRAS, 442, 2240

Appendix A: Table

Table A.1. Water masers and radio continuum.

Source	d	L_{bol}	YSO continuum [a]		N_{mas}	Maximum radius
			RA (J2000)	Dec (J2000)		
	(kpc)	($L_\odot$)	(h m s)	(° ′ ″)		(au)
G005.88−0.39	2.99 ± 0.18	5.8×10^4	18 00 30.440	−24 04 00.90	26	16 708
G009.99−0.03 [b]	*5.0*	*1.2×10^4*	18 07 50.117	−20 18 56.49	16	801
G011.92−0.61	3.37 ± 0.35	1.2×10^4	18 13 58.112	−18 54 20.19	27	776
G012.43−1.12 [b]	*3.7*	*4.2×10^4*	18 16 52.161	−18 41 43.94	3	227
G012.68−0.18	2.40 ± 0.18	5.7×10^3	18 13 54.750	−18 01 46.58	21	630
G012.90−0.24	2.45 ± 0.15	8.6×10^2	18 14 34.428	−17 51 51.80	2	130
G014.64−0.58	1.83 ± 0.07	1.1×10^3	18 19 15.546	−16 29 45.83	5	185
G016.58−0.05	3.58 ± 0.30	1.3×10^4	18 21 09.125	−14 31 48.65	35	2179
G026.42+1.69 [b]	*3.1*	*9.0×10^3*	18 33 30.508	−05 01 01.95	7	275
G031.58+0.08	4.90 ± 0.72	2.0×10^4	18 48 41.613	−01 09 57.70	11	11 484
G035.02+0.35	2.33 ± 0.22	1.0×10^4	18 54 00.649	+02 01 19.41	27	621
G049.19−0.34	5.29 ± 0.20	6.0×10^3	19 22 57.771	+14 16 09.91	11	254
G074.04−1.71	1.59 ± 0.05	*3.7×10^2*	20 25 07.117	+34 49 57.53	29	586
G075.76+0.34	3.51 ± 0.28	1.4×10^4	20 21 41.093	+37 25 29.19	19	453
G075.78+0.34	3.72 ± 0.43	1.1×10^4	20 21 44.013	+37 26 37.51	61	2439
G076.38−0.62	1.30 ± 0.09	*1.4×10^4*	20 27 25.477	+37 22 48.42	50	115
G079.88+1.18	1.61 ± 0.07	8.6×10^2	20 30 29.145	+41 15 53.54	6	178
G090.21+2.32	0.67 ± 0.02	2.7×10^1	21 02 22.703	+50 03 08.27	15	38
G092.69+3.08	1.63 ± 0.05	*(4.7×10^3)*	21 09 21.714	+52 22 37.02	50	275
G097.53+3.18–M	7.52 ± 0.96	*(8.8×10^4)*	21 32 12.451	+55 53 49.76	82	1923
G100.38−3.58	3.44 ± 0.10	*8.5×10^3*	22 16 10.365	+52 21 34.14	49	755
G105.42+9.88 [c] 3A	0.89 ± 0.05	*(5.8×10^2)*	21 43 06.474	+66 06 54.98	2	15
G105.42+9.88 [c] 3B	0.89 ± 0.05	*(5.8×10^2)*	21 43 06.460	+66 06 55.18	72	23
G108.20+0.59	4.37 ± 0.53	2.1×10^3	22 49 31.465	+59 55 41.86	39	452
G111.24−1.24	3.47 ± 0.53	*1.0×10^4*	23 17 20.891	+59 28 47.60	21	3575
G111.25−0.77	3.40 ± 0.18	*5.0×10^3*	23 16 10.331	+59 55 28.63	57	1268
G160.14+3.16	4.10 ± 0.10	*8.4×10^3*	05 01 39.914	+47 07 21.58	5	17 304
G168.06+0.82	7.69 ± 2.37	1.6×10^4	05 17 13.743	+39 22 19.85	15	1849
G176.52+0.20	0.96 ± 0.02	1.5×10^2	05 37 52.136	+32 00 03.93	71	177
G182.68−3.27	6.71 ± 0.50	*8.6×10^2*	05 39 28.419	+24 56 32.16	3	347
G183.72−3.66	1.75 ± 0.04	*9.7×10^2*	05 40 24.230	+23 50 54.68	22	117
G229.57+0.15 [d] 1	4.52 ± 0.29	2.2×10^3	07 23 01.845	−14 41 32.79	2	161
G229.57+0.15 [d] 2	4.52 ± 0.29	2.2×10^3	07 23 01.804	−14 41 32.94	26	389
G236.82+1.98	3.36 ± 0.20	*2.3×10^3*	07 44 28.239	−20 08 30.19	44	560
G240.32+0.07	4.72 ± 0.47	8.3×10^3	07 44 52.040	−24 07 42.21	10	8473
G359.97−0.46 [b]	*4.0*	*5.7×10^4*	17 47 20.188	−29 11 59.04	4	975
AFGL 5142	2.14 ± 0.05	5.0×10^3	05 30 48.018	+33 47 54.54	23	469
IRAS 20126+4104	1.64 ± 0.05	1.3×10^4	20 14 26.054	+41 13 32.49	26	865

Notes. Column 1 reports the name of the POETS targets: the two sources in italic characters have been observed prior of the POETS survey; Cols. 2 and 3 give the trigonometric parallax distance from BeSSeL (available for all but four sources, for which the kinematic distance is reported) and the evaluated bolometric luminosity, respectively: kinematic distances and more uncertain luminosities are given in italic characters, and values which might be severe upper limits are enclosed within brackets; Cols. 4 and 5 give the RA and Dec coordinates, respectively, of the YSO, pinpointed by JVLA, high-angular resolution, radio continuum observations; Cols. 6 and 7 list the number of detected maser cloudlets and the maximum maser separation from the YSO, respectively. [a]In a few cases where the continuum emission shows two nearby peaks, we choose the peak closer to most of the water masers. In three objects, G005.88−0.39, IRAS 20126+4104, and AFGL 5142, previously studied at subarcsecond resolution with millimeter and near-infrared interferometers, we have used the position of the YSO identified through continuum or molecular line emissions. [b]In this target, the water maser emission has faded away over the VLBI observing epochs, and nor trigonometric parallax distance neither reliable maser proper motions have been measured. [c]In this target, the water maser emission comes from two nearby YSOs, resolved through subarcsecond VLA observations, named VLA 3A and VLA 3B. [d]In this target, the water maser emission comes from two nearby YSOs, resolved through subarcsecond VLA observations, named VLA-1 and VLA-2.